ADVANCED FUNCTIONAL MATERIALS
www.afm-journal.de

Understanding Thermal and A-Thermal Trapping Processes in Lead Halide Perovskites Towards Effective Radiation Detection Schemes

Carmelita Rodà, Mauro Fasoli, Matteo L. Zaffalon, Francesca Cova, Valerio Pinchetti, Javad Shamsi, Ahmed L. Abdelhady, Muhammad Imran, Francesco Meinardi, Liberato Manna, Anna Vedda,* and Sergio Brovelli**

Lead halide perovskites (LHP) are rapidly emerging as efficient, low-cost, solution-processable scintillators for radiation detection. Carrier trapping is arguably the most critical limitation to the scintillation performance. Nonetheless, no clear picture of the trapping and detrapping mechanisms to/from shallow and deep trap states involved in the scintillation process has been reported to date, as well as on the role of the material dimensionality. Here, this issue is addressed by performing, for the first time, a comprehensive study using radioluminescence and photoluminescence measurements side-by-side to thermally-stimulated luminescence (TSL) and afterglow experiments on $CsPbBr_3$ with increasing dimensionality, namely nanocubes, nanowires, nanosheets, and bulk crystals. All systems are found to be affected by shallow defects resulting in delayed intragap emission following detrapping via a-thermal tunneling. TSL further reveals the existence of additional temperature-activated detrapping pathways from deeper trap states, whose effect grows with the material dimensionality, becoming the dominant process in bulk crystals. These results highlight that, compared to massive solids where the suppression of both deep and shallow defects is critical, low dimensional nanostructures are more promising active materials for LHP scintillators, provided that their integration in functional devices meets efficient surface engineering.

1. Introduction

The interaction between high-energy radiation and matter is a unique tool to investigate fundamental processes in particle and high-energy physics and underpins relevant technological applications in numerous fields including homeland security, industrial and medical imaging, safety screening, and quality inspection in food industry.[1] Radiation detection strategies have been the subject of a large body of research, leading to the development of both direct radiation-to-charge converters and scintillator-based detectors,[2] where ionizing radiation is first converted into UV-visible light, which is then collected and turned into an electrical signal by coupled photomultipliers or solid-state diodes. Efficient scintillator detectors require dense active materials to ensure high interaction probability with ionizing radiation ($P_i \propto Z^n$ that scales with the n^{th} power of the effective atomic mass Z, with n = 1–5 depending on the type of interaction),[3] and high emission yield, which is typically optimized by minimizing the defect concentration in high optical quality single crystals. The fabrication of massive defect-free scintillation crystals, however, requires high-temperature crystallization processes, which complicate the realization of upscalable large-area devices and hinder their integration on flexible substrates. For this reason, solution-processable materials such as semiconductor or oxide nanocrystals[4] represent an attractive alternative as active layers for a new generation of low-cost and versatile radiation detectors.[5]

Very recently, all-inorganic ($CsPbX_3$, X = Br, I, Cl) and hybrid organic-inorganic ($APbX_3$, A = methylammonium, MA; formamidinium, FA) lead halide perovskites (LHP) have emerged as promising candidates for efficient X- and γ-ray detection.[2b,6] These materials combine affordable, low-temperature solution processing with strong light-matter interaction posited by their lead-based composition[2b,7] and large electron-hole diffusion length.[2b,6b] Specifically, owing to their high stopping power[2b,6b,8] and efficient direct conversion of ionizing radiation into charge carriers,[2b,6b,9] bulk $MAPbI_3$ perovskites have

C. Rodà, M. Fasoli, M. L. Zaffalon, F. Cova, V. Pinchetti, F. Meinardi, A. Vedda, S. Brovelli
Dipartimento di Scienza dei Materiali
Università degli Studi Milano Bicocca
via R. Cozzi 55, Milano IT-20125, Italy
E-mail: anna.vedda@unimib.it; sergio.brovelli@unimib.it

J. Shamsi, A. L. Abdelhady, M. Imran, L. Manna
Istituto Italiano di Tecnologia
via Morego 30, Genova IT-16163, Italy
E-mail: liberato.manna@iit.it

The ORCID identification number(s) for the author(s) of this article can be found under https://doi.org/10.1002/adfm.202104879.

DOI: 10.1002/adfm.202104879

shown sensitivity values higher than conventional α-Se detectors (10^4 μC $Gy_{air}^{-1}cm^{-2}$). This allows us to reduce the dose exposure, a critical parameter in medical applications.[8b] Similarly, planar devices based on $CsPbBr_3$ bulk single crystals (BSCs) have shown energy resolution comparable to commercial γ-ray CdZnTe detectors.[6b] In addition to this, LHP crystals show strong and fast radioluminescence (RL) due to the recombination of band-edge (BE) exciton, promoting their implementation as low-cost scintillators.[7,10] Colloidal synthesis routes for LHP nanocrystals have further opened up to the demonstration of color-tunable scintillators, achievable by tailoring the BE exciton recombination energy via particle size control[11] and anion composition.[12] As a result, $CsPbX_3$ nanocrystals featuring efficient and narrow-band RL across the whole visible spectrum have been reported.[5b,9b] This aspect represents a significant advancement with respect to conventional scintillators, such as thallium activated CsI and cerium-activated single crystals like $YAlO_3$ perovskites, silicates, and mixed garnets,[13] where the emission energy is dictated by the chemical composition of the activator and the matrix materials. Notably, LHP nanostructures are easily processed into films at room temperature, which has enabled the fabrication of low-cost flexible scintillators based on $CsPbBr_3$ nanocubes (NCs)[14] and nanosheets (NSs).[15] More recently, $CsPbBr_3$ nanocrystals have also been employed as an efficient high-Z sensitizer for organic dyes in plastic scintillators, enabling the demonstration of fast and re-absorption free scintillation with efficiency comparable to commercial bulk crystals.[16]

All these ground-breaking advancements highlight the potential of LHP materials as active components of new, efficient, and affordable radiation detectors. Despite this promise, there are still important aspects that determine the performance of LHP crystals and nanostructures in radiation detection that have not been investigated in detail yet. In particular, little is known of the thermodynamics and kinetics of trapping and detrapping mechanisms of carriers generated upon interaction with ionizing radiation in shallow and deep defects which are both responsible for relevant, and typically detrimental, effects on the scintillation process. Specifically, shallow traps with longer but comparable lifetime to the scintillation decay-time are known to compromise the time-resolution of scintillators causing slow scintillation tails due to slow detrapping.[17] On the other hand, deep traps—, that is, localized electronic states with a lifetime much longer than the scintillation decay time—trap carriers in a stable and irreversible way (except upon the delivery of the necessary energy budget), thereby reducing the scintillation efficiency.[18] Finally, intermediate trapping behaviors can also be present, leading to millisecond long RL decay tails commonly referred to as afterglow (AG).[17a,19] While recent reports investigated a seemingly ubiquitous low-temperature trap emission in the photoluminescence (PL)[20] and RL[10b] spectra of $CsPbBr_3$ nanostructures and BSCs, no information concerning non-radiative intermediate and deep traps is available in the literature, as well as on the role of the material dimensionality on the trapping and detrapping processes.

In this work, we aim at contributing to this task by combining PL and RL experiments as a function of temperature (T), side-by-side to thermally-stimulated luminescence (TSL), and low-temperature AG measurements to investigate the trapping and detrapping processes involved in the scintillation of $CsPbBr_3$ perovskite nanostructures of increasing dimensionality, namely NCs, nanowires (NWs), NSs, along with the respective BSC. In order to explore the role of surface and bulk defects through control of the surface-to-volume ratio (*S:V*), with minimal spurious effects due to particle quantum confinement, we specifically selected nanostructures larger than the excitonic Bohr radius of $CsPbBr_3$ (a_B = 3.5 nm).[11a] RL experiments between 10 and 320 K revealed the emergence, for $T < 70$ K, of an intragap luminescence band due to radiative recombination of excitons in shallow traps in any of the investigated systems. Continuous-wave (CW) and time-resolved PL experiments showed comparable emission trends, indicating that X-ray irradiation does not produce photo-generated defects in any LHP system and pointing to the thermal exchange between shallow-trapped and BE excitons. Differently from RL and PL experiments where the investigated timescale is comparable to the lifetime of the BE excitons, TSL and AG allow to probe the delayed-emission of detrapped carriers from deep centers and, notably, also the dynamics of non-radiative traps, thus providing a complementary experimental tool to RL and PL for a comprehensive analysis of the trapping and detrapping processes in both deep and shallow trap states. TSL and AG experiments at cryogenic temperature revealed a strong correlation between the system dimensionality and the detrapping mechanism from deep non-radiative traps. Specifically, the TSL glow curve of the BSC—and similarly, but with lower intensity for the NWs and NSs—shows an intense peak at T = 112 K marking the thermal activation of exciton detrapping which is not observed in the lower dimensional NCs. Finally, AG measurements at T = 10 K combined with TSL shed light onto the nature of the prolonged TSL decay common to all investigated LHP materials whose emission energy matches the low-T intragap RL and PL, revealing that in all nanostructures the main detrapping pathway is a-thermal tunneling towards a trapped excitonic state. Altogether these results point out that, despite their defect tolerant band structure,[21] the BE exciton/carriers in LHPs are substantially impacted by traps that are likely associated with surface defects. In addition to that, lowering the *S:V* ratio leads to a progressive emergence in NWs and NSs of the signatures of a deep localized state possibly placed inside the particle volume that becomes the dominant trapping channel in BSC. Such a deeper understanding of the defect physics in LHPs offers valuable guidelines for future realization of efficient LHP-based radiation detectors.

2. Results and Discussion

2.1. RL Experiments as a Function of Temperature

The systems investigated in this work were produced following the protocols reported in the Experimental Section. In all nanostructures, the particle dimensions are larger than the exciton Bohr radius of $CsPbBr_3$ (a_B = 3.5 nm),[11a] resulting in a weak quantum confinement effect. Specifically, the average lateral size of the NCs is 9 ± 2 nm, the NWs are 11 ± 1 nm wide and over 500 nm long and the NSs are 20 ± 2 nm thick with lateral size up to 1 μm, as extracted from the transmission electron microscopy (TEM) images (Figure S1, Supporting Information). Accordingly, the PL spectra at 300 K of all nanostructures in toluene solution (Figure S2, Supporting Information) are characterized by an almost negligible blue-shift of the PL peak with

respect to the BSC (≈2.38–2.42 eV vs ≈2.36 eV), featuring the characteristic narrow full width at half maximum (FWHM) values (< 80 meV) typical of $CsPbBr_3$ perovskite materials.[11a] The PL quantum yield (Φ_{PL}) of the NCs, NWs, and NSs amounts to 10±2%, 10±2%, and 20±4% respectively. The BSC shows $\Phi_{PL} < 1\%$, consistent with the large exciton diffusion length in perovskite single crystals leading to a more dominant effect of nonradiative trapping compared to nanostructures. Excluding quantum confinement effects allow us to focus on the impact of the *S:V* by decreasing the dimensionality of the systems. Specifically, moving from the BSC, where the effect of the surface is negligible ($S{:}V = 6 \times 10^{-6}$ nm^{-1}) to the NSs ($S{:}V = 2 \times 10^{-3}$ nm^{-1}) the contribution of the surface becomes dominant in NWs ($S{:}V = 0.1$ nm^{-1}) and NCs ($S{:}V = 0.7$ nm^{-1}).

We start our analysis by performing RL and PL measurements as a function of temperature for all nanostructures and the BSC. The normalized RL spectra of all systems versus *T* are reported in **Figure 1**a; the respective PL spectra are shown in

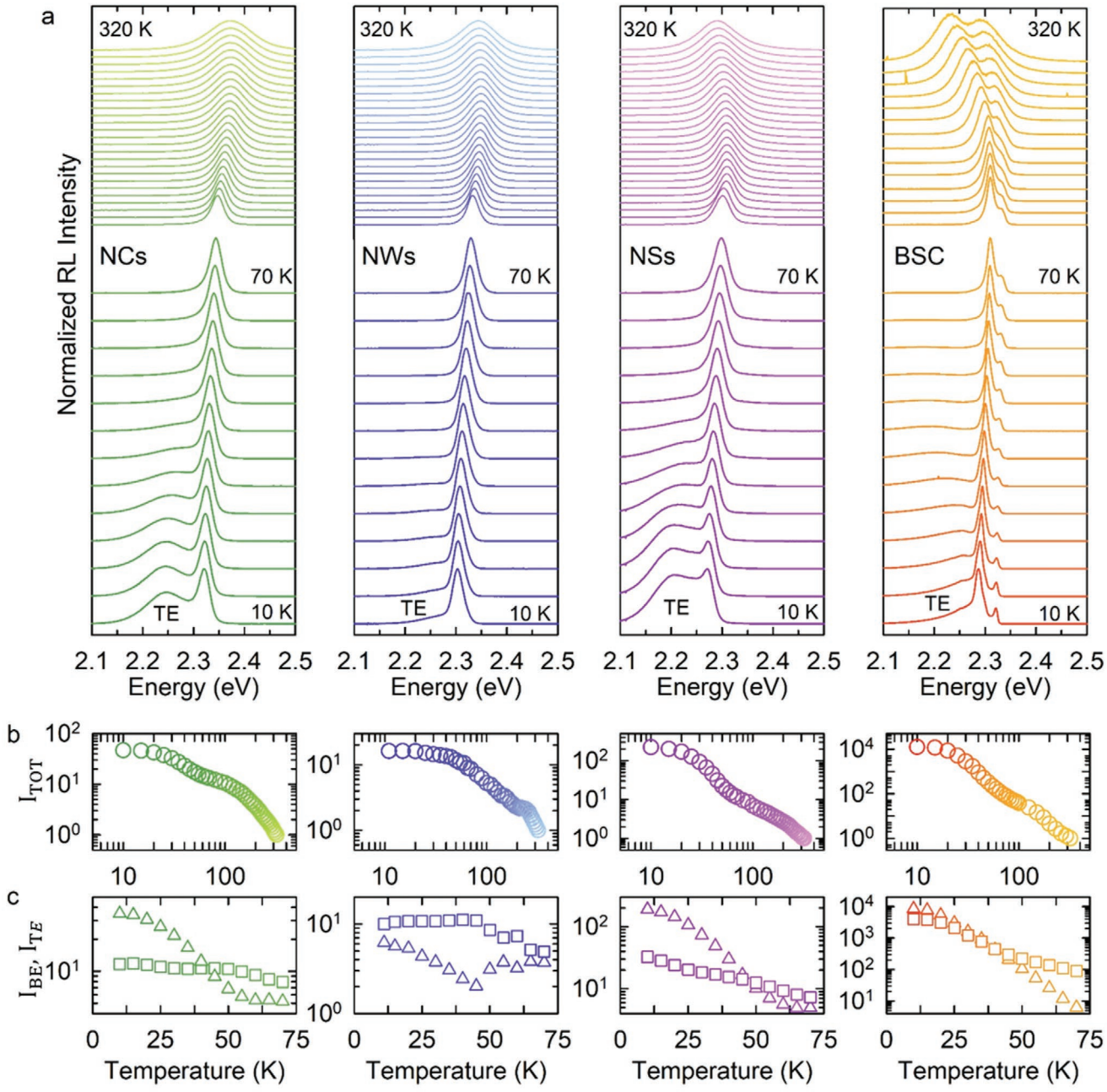

Figure 1. RL of $CsPbBr_3$ nanostructures and single crystal. a) Normalized RL spectra as a function of temperature from 10 (bottom) to 320 K (top) for $CsPbBr_3$ NCs (green), NWs (blue), NSs (violet), and BSC (orange). The curves have been offset for clarity. b) Total integrated RL intensity (I_{TOT}) as a function of temperature and c) weight of the BE ($I_{BE,}$ squares) and TE ($I_{TE,}$ triangles) integrated RL intensities calculated with respect to I_{TOT}. I_{BE} of the BSC takes into account the evolution of both spectral components detected at room-*T*. I_{TOT} is normalized to its value at 320 K. All samples were excited by a continuous distribution of X-rays produced by Bremsstrahlung with maximum energy at 32 keV.

Figure 2a for the NCs and Figures S3–S5, Supporting Information, for the other samples. At room temperature, all nanostructures show a single RL peak (at 2.37, 2.35, and 2.30 eV for NCs, NWs, and NSs respectively) due to the recombination of BE excitons nearly matching the respective PL excited at 3.06 eV. The BSC shows a single peak PL (Figure S2, Supporting Information) and a structured RL (Figure 1d) profile with two spectral components respectively at 2.23 and 2.29 eV, consistently with previous reports on lead-based perovskite BSCs and thin films with different compositions of the A-site cations.[2b,10b,22] To date, no general agreement on the nature of such spectral structure has been reached in the literature. Possible origins include biexciton recombination,[22b] phonon replica,[22d] bulk versus surface recombination,[2b,22e] re-absorption and self-absorption effect,[22a,f] and recombination of exciton bound to a halide vacancy.[22c] More recently, this effect has been assigned to polar distortion of the $PbBr_6$ octahedrons at high temperature, giving rise to indirect tail states below band-gap due to dynamical Rashba splitting effect.[22b] We point out that at cryogenic temperatures the BSC reveals the composite nature of its BE-PL emission (Figure S5, Supporting Information), according to the RL spectra.

Upon reducing the temperature, for all systems, we observe a progressive spectral narrowing (25–90 meV) of the excitonic peak due to the gradual suppression of homogeneous broadening[20b,22c,23] and the typical redshift of the exciton position at low T.[20b,23b,24] Nonetheless, whereas the exciton peak of the NCs shows monotonic redshift for $T < 250$ K (≈50 meV from 300 to 5K), the RL of higher dimensional systems is characterized by an initial blue-shift (NWs +5 meV, NSs +19 meV, BSC + 80 meV, and +40 meV) approaching $T = 70$ K that is overtaken by a 20–80 meV redshift at lower temperatures. Such a non-monotonic trend of the band-gap energy can be rationalized by the competition between electron-phonon coupling and temperature-induced changes in the lattice potential of LHP materials[23b,24,25] whose effect is enhanced in higher dimensional samples. More interestingly for our study, as highlighted in Figure 1a, for $T < 70$ K an additional broad

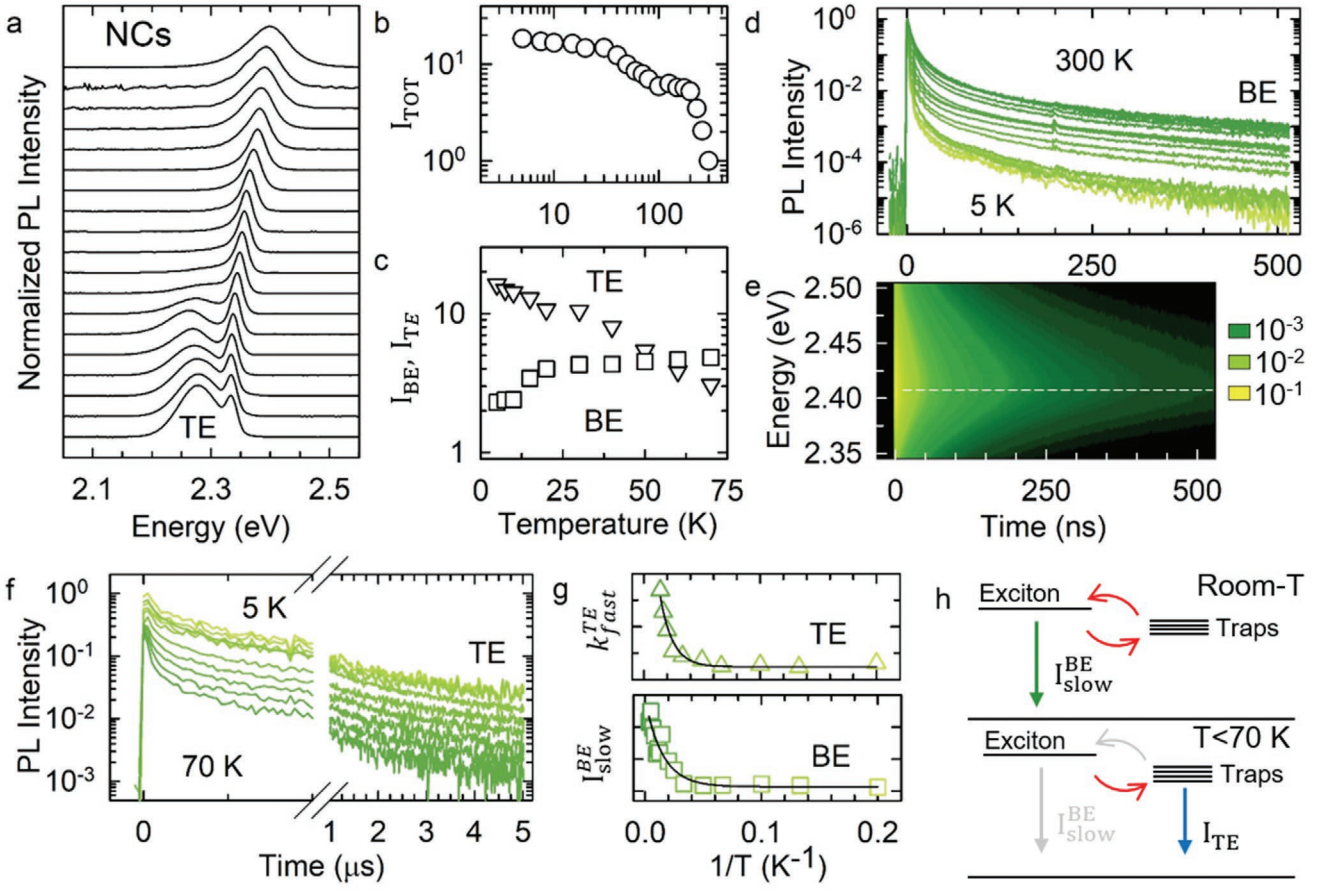

Figure 2. CW and time-resolved PL of $CsPbBr_3$ NCs between 5 and 300 K. a) PL spectra as a function of temperature from 5 (bottom) to 300 K (top). b) Total integrated PL intensity (I_{TOT}) as a function of temperature and c) weight of the BE- (I_{BE}, squares) and TE- (I_{TE}, triangles) integrated PL intensities between 5 and 70 K. d) Normalized PL decay curves of the BE-PL as a function of the temperature from 300 to 5 K. e) Contour plot of the spectrally-resolved BE-PL decay at 300 K. f) TE-PL decay curves as a function of the temperature between 5 and 70 K. The data are normalized for the time zero TE-PL intensity at 5 K. g) Temperature dependence of the decay rate of the fast TE-PL component (k_{fast}^{TE}) and the relative weight of the slow component of the BE-PL decay curves (I_{Slow}^{BE}), together with their respective fit using Equations (1) and (2) h) Schematic depiction of the T-dependent dynamics. At room-T the TE can repopulate the BE via thermally assisted detrapping, giving rise to a delayed component in the BE-PL emission I_{Slow}^{BE} (green arrow). For $T < 70$ K, the detrapping is progressively inhibited leading to the direct emission from the TE states I_{TE} (blue arrow) and consequent decrease of I_{Slow}^{BE}. All samples were excited at 3.06 eV.

(FWHM≈40–70 meV) sub-bandgap emission redshifted with respect to the BE emission peak (70 meV NCs, 59 meV NSs, 32 meV NWs, 15 meV BSC at 10 K) progressively emerges in both the RL and PL spectra of all systems, which we ascribe to the radiative recombination of trapped excitons (TE) in a manifold of shallow traps, in agreement with previous PL[20] and RL[10b] studies. The observation of such a TE-RL band for both the BSC and related nanostructures featuring much larger S:*V* suggests that similar defects are found in both the bulk and the surfaces of $CsPbBr_3$ systems.

In Figure 1b we report the temperature dependence of the total integrated RL intensity (I_{TOT}). The same analysis of the PL data is reported in Figure 2b for the NCs and in Figure S6, Supporting Information, for the other samples, showing essentially identical trends as the RL data for all investigated systems. In all cases, I_{TOT} grows by at least a factor of ten with decreasing temperature from 320 to 10 K. By monitoring the BE and TE emissions separately as quantified in Figure 1c, where we report the weight of their RL integrated intensity (I_{BE}, I_{TE}), we notice that for all systems, the BE emission grows and reaches saturation when the temperature is decreased from 320 to 70 K. On the other hand, for T< 70 K the increase of I_{TOT} is mostly due to the growth of the TE-RL intensity, which becomes the dominant contribution in the case of NCs, NSs, and BSC. The NWs follow a similar trend as the other systems, although with a markedly lower contribution by the TE at low *T*.

2.2. CW- and Time-Resolved PL Experiments as a Function of Temperature

To understand the origin of the thermal behavior of the BE and the TE recombination channels, we performed CW and time-resolved PL experiments in the 5–300 K temperature range. Since all investigated $CsPbBr_3$ systems showed very similar PL versus *T* trends, we focused our discussion on the NCs as a representative example. The time-resolved PL data of the other samples are reported in Figures S7–S9, Supporting Information. In Figure 2a we report the PL spectra of the NCs between T = 5 K and T = 300 K. Consistent with the RL data, the room temperature PL spectrum is dominated by the BE emission at 2.4 eV. Upon cooling, the PL gradually intensifies (Figure 2b), and the PL spectrum undergoes very similar narrowing and redshift as observed for the RL. For T < 70K, a broad TE emission identical to the RL shown in Figure 1a arises and becomes progressively dominant, as quantified in Figure 2c where we report the weight of the BE- and TE-PL integrated contributions. The close match between the PL spectra and the respective RL profiles, as well as the trends of their intensity versus *T*, indicate that the shallow defects responsible for the TE emission were not generated upon X-ray irradiation. In Figure 2d we report the PL time-decay curves of the BE between 5 and 300 K, showing a fast component with effective lifetime τ_{Fast}^{BE} = 6 ns (accounting ≈80% of the signal at room temperature) followed by a long-lived tail with decay time τ_{Slow}^{BE} ≈ 150 ns. In order to clarify the origin of the delayed-PL, in Figure 2e we report the contour plot of the spectrally-resolved PL-decay of the NCs at 300 K, showing essentially the same emission profile over the entire decay time and thus confirming that the fast and the long-lived component originate from the same exciton state. Notably, the fast component of the BE shows progressive acceleration with decreasing temperature (Figure S10, Supporting Information) according to the bright nature of the triplet excitonic states in LHP nanostructures,[26] in stark contrast to τ_{Slow}^{BE} that remains essentially constant throughout the whole temperature range (Figure S11, Supporting Information). Consistent with previous reports,[27] we ascribe the fast component of the PL decay to recombination of photoexcited BE excitons and the longer-lived one to delayed emission of thermally regenerated BE excitons by detrapping from shallow-trap states. To assess whether such trap states are also involved in the TE emission observed under both photo and X-ray excitation, we analyzed the temperature evolution of the TE decay dynamics. The TE-PL decay curves (Figure 2f) are featured by an initial faster contribution with lifetime τ_{Fast}^{TE} ≈100 ns at 5 K followed by a µ-second long decay component. We assign the fast recombination channel of the TE states to the non-radiative recombination of TE by thermally assisted detrapping to the BE state, while the µ-second component corresponds to the direct radiative recombination of the TE when no transfer of carriers takes place.

Accordingly, upon lowering the temperature, the decay rate of the fast TE-PL component (k_{fast}^{TE}) drops (Figure 2g), in compliance with the idea of progressively inhibited detrapping by back-transfer to the BE state. Consistently, such a decrease in k_{fast}^{TE} is accompanied by a concomitant decrease of the relative weight of the slow decay contribution of the BE-PL (I_{slow}^{BE}) due to re-populated BE excitons (Figure 2g), giving definitive proof of the thermally driven interchange taking place between the two states, as depicted in Figure 2h. According to this picture, we evaluated the detrapping energy E_{DT} by fitting the temperature dependence of I_{slow}^{BE} and k_{fast}^{TE} respectively with the expressions

$$I_{slow}^{BE} = I_0\, e^{-\frac{E_{DT}}{k_B T}} \quad (1)$$

$$k_{fast}^{TE} = k_0 + k_1 e^{-\frac{E_{DT}}{k_B T}} \quad (2)$$

both consistently yielding E_{DT} = 6–8 meV. We notice that the same analysis carried out for the NWs (Figure S12, Supporting Information) leads to an activation energy of only 2 meV, suggesting that even at cryogenic temperature the detrapping is highly efficient in this system. This aspect could originate from the peculiar behavior of NWs to merge into larger structures, affecting the coordination of surface sites and defects, and could explain the lower contribution of the TE emission in NWs compared to the other samples (Figure 1, Figure S6, Supporting Information). Finally, we point out that the energy shift between the BE-PL and the TE-PL at 5K (≈50 meV) is much higher than the activation energy of the back-transfer, suggesting that the radiative recombination of TE takes place from the bottom of a manifold of states.

2.3. TSL and Low-*T* AG

Next, we proceed in our analysis by performing TSL and low-*T* AG measurements for all investigated systems. TSL and AG

are powerful techniques largely employed in the field of scintillation and dosimetry, as they specifically probe the dynamics of detrapping processes from defect states. Specifically, a typical TSL experiment consists of two steps. First, the sample is exposed to prolonged X-ray irradiation at a given temperature to populate trap states in the bandgap that are stable at the chosen temperature. Successively, the irradiation is interrupted, and the sample is progressively heated using a linear heating rate while monitoring the delayed emission due to carrier detrapping. This allows one to correlate the temperature at which a specific TSL peak is detected with trap parameters like trap depth (ΔE_T) and attempt-to-escape frequency (or frequency factor) s. In AG measurements, X-ray irradiation is performed analogously but the sample is kept at a constant temperature during the whole acquisition of the delayed emission; in a thermally assisted detrapping process, the decay time, τ_T, of the delayed emission is related to trap parameters by the formula:

$$\tau_T = \frac{1}{s}\exp\left(\Delta E_T / k_B T\right) \tag{3}$$

where s is the frequency factor that is related to the temperature of the maximum TSL peak, T_M, and to the heating rate β by

$$s = \frac{\beta E_T}{k_B T_M^2}\exp\left(\Delta E_T / k_B T_M\right) \tag{4}$$

Based on this, we proceeded with TSL experiments by irradiating the samples at 10 K for 15 min, after which the temperature was linearly increased with a heating rate of 0.1 K s^{-1}. In **Figure 3**a we report the contour plots of the spectrally resolved TSL intensity of all investigated samples as a function of temperature. All systems exhibit a broad (1.7–2.5 eV) monotonic TSL emission extending over a wide range of temperatures. For the BSC, such a monotonically decreasing TSL signal is superimposed to an intense TSL peak emerging at 112 K.

A closer look at the contour plot of the NSs and the NWs reveals an analogous, yet substantially weaker, signal emerging at T = 112 K. In order to resolve the spectral contribution to the TSL contour plot, in Figure 3b we report the TSL spectra integrated over two temperature intervals, namely T < 90 K and 90 K < T < 130 K. The low-T TSL spectra of all systems are substantially similar, with a main narrow peak at ≈2.25 eV that matches the TE-RL and PL discussed in Figure 1 and Figure 2. Interestingly, the BE emission is lacking in all systems while a low-energy shoulder extending to 1.5 eV (TE'), whose relative intensity increases with the system dimensionality, is detected altogether with TE above 90 K, in the region of the 112 K peak. Upon heating, TE' intensifies, with the higher dimensional system showing the largest growth, resulting in a featureless TSL spectrum at 1.9 eV dominating the spectrum of the BSC. Such features, namely the presence of a sharp peak and of an additional emission center below 2 eV, and their strong anticorrelation with S:V, suggest the existence of different trap-center recombination paths that will be discussed in detail in **Figure 4**.

Once we analyzed the spectral composition of the emitting centers, we proceeded to investigate the kinetics of the detrapping mechanisms. In Figure 3c we report the spectrally-integrated TSL intensity as a function of the temperature (commonly referred to as "glow curves") for all investigated samples. Since in TSL experiments temperature and time are linearly correlated, we can map the decay of the TSL intensity as a function of time, as shown in Figure 3c. Consistent with the respective TSL contour plots, the glow curves of the nanostructures decrease monotonically with temperature (time) and the NWs and NSs show an additional peak at 112 K (insets in Figure 3c), corresponding to the rise of TE' in the TSL spectra in the 90–120K temperature range. According to the above discussion, the BSC shows essentially the same monotonic behavior of the nanostructures with an additional peak at 112 K, almost ten times more intense than the underlying TSL intensity trend, followed by a weaker peak at 135 K. The emergence of TSL peaks in glow curves is the typical signature of a thermally activated detrapping process.[28] Specifically, the rise of the TSL corresponds to the onset of carrier release from a trap. Once a significant portion of the traps has been emptied, the TSL signal starts to decrease, leading to a typical peak feature in the glow curve.

Before investigating the energetics of the TSL peaks, we analyze the monotonic decay of the TSL intensity common to all samples. We choose to focus on the NCs, since no TSL peaks are detected in their glow curve. In Figure 3d we report the inverse of the TSL intensity in the first 15 min after suppression of the irradiation (10–100 K), showing a clear linear trend with time. Notably, such a linear behavior is the typical signature of direct a-thermal tunneling of trapped carriers from a distribution of trap-center distances.[29] In this case, the release of carriers is not mediated by the material bands, but it is instead due to direct tunneling from the trap state to an excited state of the luminescent center positioned at the same energy. Accordingly, we fit the data using the expression,

$$I(t) = A\left(t + t_0\right)^{-p} \tag{5}$$

that yields $p = 1.01 \pm 0.06$ for NCs, in excellent agreement with a-thermal tunneling release of carriers.[29c] Moreover, in order to further confirm the presence of a-thermal tunneling, we performed AG measurements at T = 10 K on NSs and BSC, where the thermal contribution is more pronounced.

In Figure 4a we report the spectrally integrated TSL intensity together with the AG intensity as a function of time for the NSs and BSC. Both samples show prolonged delayed emission at constant T = 10 K, definitely proving the presence of an a-thermal detrapping channel. Accordingly, fitting the AG decays with Equation (5) yields $p = -0.90 \pm 0.01$ for NSs and $p = -0.99 \pm 0.02$ for the BSC, and the AG spectra (Figure 4b) show constant shape with time for both systems. Notably, the low-temperature TSL spectra (Figure 3b) closely resemble the AG spectra, except for the low-energy contribution responsible for the TSL peaks of the AG curves. We point out that the trap that transfers via tunneling is situated at the same energy of the excited state of the emitting center, since tunneling occurs exclusively between isoenergetic states.

Finally, we focus on the energetics of the trap associated with the TSL peak at T = 112 K mostly observed for the BSC. To this aim, we subtracted the AG contribution from the glow

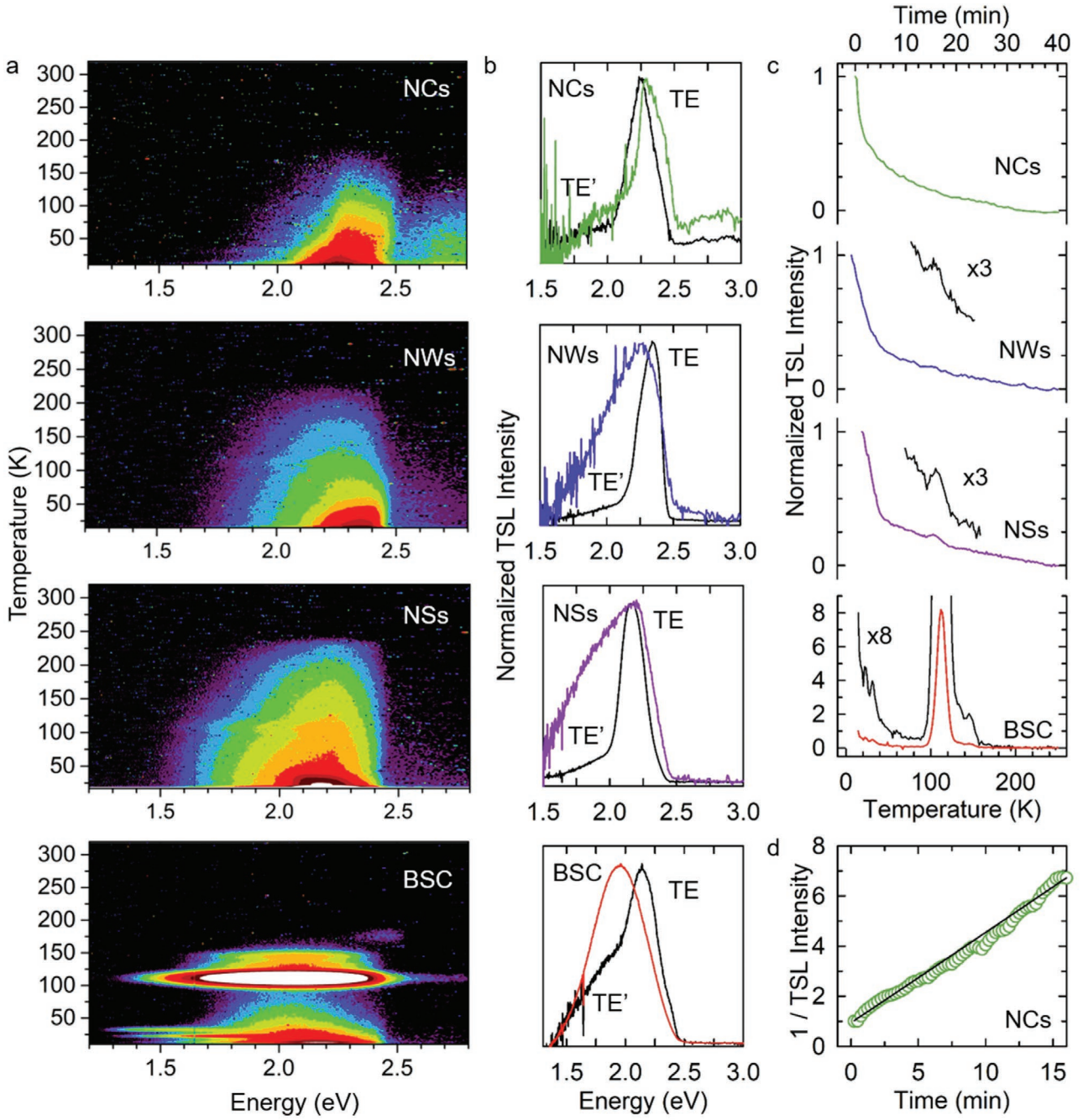

Figure 3. TSL of $CsPBr_3$ nanostructures and single crystal. a) Contour plots of the spectrally resolved TSL intensity as a function of temperature in the 10–320 K range of all investigated samples. b) Normalized spectra of the TSL intensity integrated for $T < 90$K (black curve) and between 90 and 130 K (colored curve). c) Glow curves of all investigated samples normalized for their initial value at $T = 10$ K. The black insets in Figure are a magnification of the glow curve to highlight the TSL peak of NWs and NSs and the initial monotonic decay of the BSC. d) Inverse of the TSL intensity of NCs as a function of the time-delay after the suppression of irradiation. The black line is the result of the fitting to Equation (5).

curve of the BSC and calculated ΔE_T and its τ_T at room-T by the so-called initial rise method.[28,30] Specifically, ΔE_T can be evaluated by fitting the initial portion of the glow curve with the function,

$$I(T) = I_0 e^{-\frac{\Delta E_T}{k_B T}} \quad (6)$$

where I_0 is proportional to the frequency factor s. In Figure 4c we report the Arrhenius plot of the TSL amplitude in the region of interest with the respective fit, leading to $\Delta E_T = 260$ meV, a value much larger than the thermal energy at room-T.

Combining Equations (3) and (4) we obtain $s = 10^{10}$ s^{-1} and $\tau_T = 2.6$ μs at room-T, a value substantially exceeding the typical exciton recombination time of LHPs.

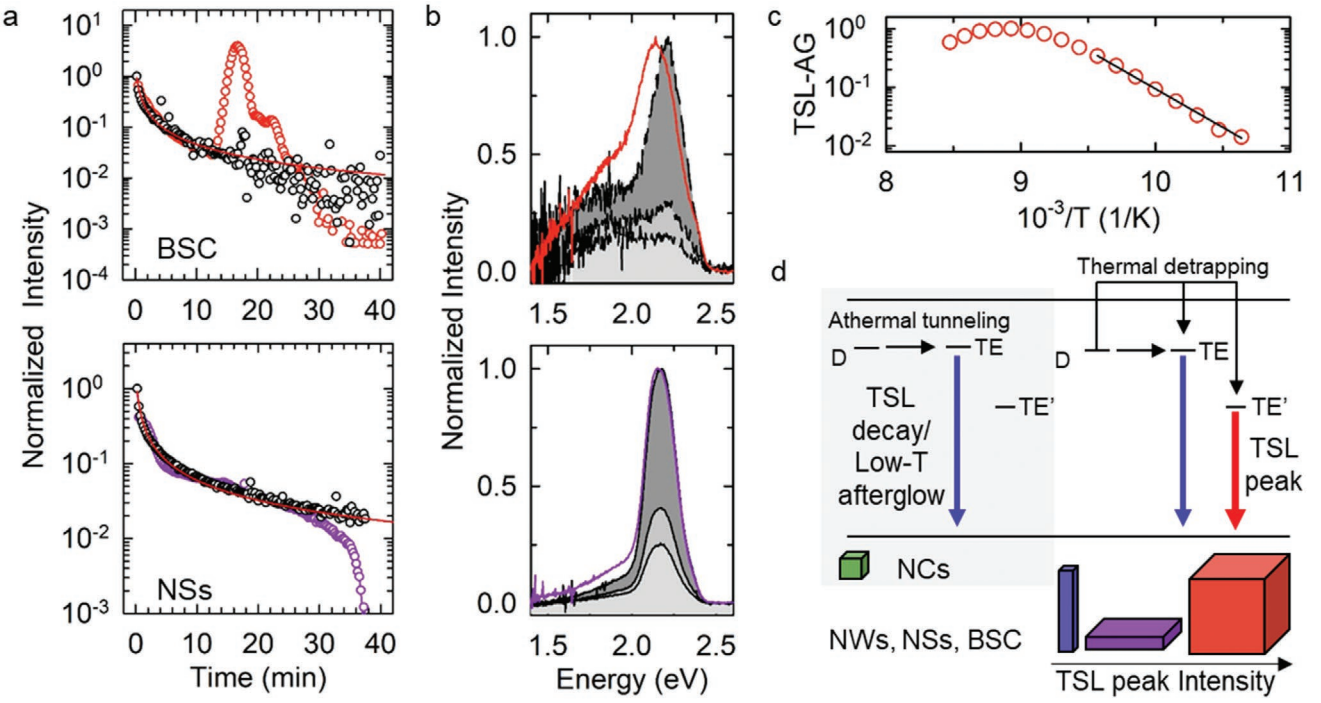

Figure 4. a) TSL intensity (red and purple circles) and AG intensity (black circles) of BSC and NSs as a function of the delay-time after suppression of the irradiation, together with the fit (red lines) of the AG intensity using Equation (5). b) Low-*T* TSL spectra (colored curves) together with the AG spectra for increasing delay-time of BSC and NSs at t = 0, t = 1.5, and t = 3 min. c) Arrhenius plot and fit (black line) of the 112 K TSL peak of BSC. d) Schematic depiction of the detrapping mechanisms observed in TSL and AG experiments. All samples are characterized by a monotonic TSL decay (blue curve) that we assign to a-thermal tunneling accordingly to low-*T* AG measurements. Such a mechanism is the unique detrapping channel in NCs, in contrast to higher-dimensional systems where an additional thermal activated detrapping mechanism takes place, leading to progressively more intense TSL emissions (red arrows) being the dominant feature in the TSL glow curve of the BSC.

Altogether the combined use of TSL and low-*T* AG experiments reveals a substantial difference in the ultra-slow detrapping mechanisms of NCs compared to higher dimensional systems, as schematically depicted in Figure 4d. In NCs, trapped carriers are mostly released via a-thermal tunneling to the same TE state observed in RL and PL experiments, leading to a monotonic decay of the TSL intensity and AG. An additional thermal detrapping channel gives rise to a TSL peak whose intensity is progressively enhanced in NWs and NSs, becoming the dominant feature of the TSL of the BSC. At variance with tunneling, characterized mostly by the selective TE emission, thermal detrapping brings carriers in delocalized states from which they can recombine evenly at two emission centers, namely TE and TE' responsible for the low energy band below 2 eV. The presence of a TE' below 2 eV also at 10 K might be due to weak thermal liberation of traps also at this temperature, which is obviously strongly enhanced when the temperature gets close to 112 K. The observed sharp decrease of the TSL just after the TSL peak at 112 K (see Figure 4) suggests that the same kind of trap is responsible for both a-thermal tunneling and TSL peak at 112 K, this last peak representing the thermally-assisted liberation of carriers leading to their complete depletion. Due to the much stronger dependence of trap-center distance in tunneling phenomena with respect to thermally assisted ones, the more pronounced relative intensity of tunneling with respect to thermal liberation in nanostructures with respect to BSC points to a greater spatial correlation between traps and emission centers in nanostructures, that are more defective due to their high *S:V*. Finally, such a picture even suggests the possibility to probe the defectivity level of nanostructures prepared by different synthesis methods by monitoring the relative weight of tunneling with respect to thermal liberation in TSL recombination.

3. Conclusions

In summary, we performed a comparative and in-depth investigation of the trapping and detrapping mechanisms of excitons in $CsPbBr_3$ perovskites of increasing dimensionality. Our results reveal that all our systems show detrapping physics related to shallow localized states due to surface defects. RL and PL measurements at various temperatures shed light on the thermal equilibrium between photogenerated excitons and localized shallow states in all investigated systems leading to delayed emission due to BE re-population following detrapping. Such a detrapping process is characterized by a thermal onset of a few meV (5.6 meV for NCs), leading to direct emission from the TE for $T < 70$K and resulting in a broad intragap RL and PL at low *T*. Interestingly, we further observe a prolonged TSL intensity decay common to all samples. This evidence combined with AG experiments allows us to assign such a prolonged luminescence to a-thermal tunneling detrapping, that appears as the principal detrapping mechanism in $CsPbBr_3$

nanostructures. Nevertheless, for NWs and NSs a TSL peak at $T = 112$ K emerges due to an additional temperature-activated detrapping channel from a deeper state (≈260 meV) with a room temperature lifetime of 2.6 µs. Our results offer valuable insights for understanding and control of traps in the scintillation of LHP materials and highlight NCs as arguably superior candidates as scintillator materials compared to higher dimensional analogs, where the suppression of defects needs to be operated both on the surface and at a volume level.

4. Experimental Section

Materials: Cesium carbonate (Cs_2CO_3, reagentPlus, 99%), 1-octadecene (ODE, technical grade, 90%), oleylamine (OLA, 70%), oleic acid (OA, 90%), 2-propanol (IPA, anhydrous, 99.5%), and toluene (anhydrous, 99.8%) and octylamine (OctAm 99,5%). Cesium bromide (99.9% trace metals basis), lead bromide (98%), dimethyl sulfoxide (99.9%). All the chemicals were purchased from Sigma-Aldrich and were used without any further purification.

Synthesis of $CsPbBr_3$ Nanostructures and Single Crystals: $CsPbBr_3$ NCs were synthesized by a colloidal procedure similar to the one reported by Protesescu et al.[11a] $CsPbBr_3$ NWs were synthesized by a colloidal procedure reported elsewhere[11b] with the difference being that the synthesis was carried out in air and without any pre-dried chemicals or solvents. Rectangular $CsPbBr_3$ NSs were synthesized by an evolution of the synthesis reported by Shamsi et al.[11c] A 4 mL $PbBr_2$ solution (0.725 g of $PbBr_2$ were dissolved in 10 mL of ODE together with 5 mL of OLA and 5 mL of OA at 100 °C) was mixed with 2 mL of ODE and 0.5 mL of an as-prepared Cs-OA precursor (325 mg of Cs_2CO_3 dissolved in 5 mL of OA by a heat gun). After adding 250 µL of IPA, the solution was stirred using a vortex for 30 s. Then the turbid greenish solution was transferred to a glass Petri dish and placed in the microwave oven (Panasonic NN-E201WM) at high power (700 W) for 5 min. Next, the reaction mixture was slowly cooled to room temperature by the water bath. To collect the NSs, 3 mL of toluene was added to the crude solution; then the mixture was centrifuged at 2000 rpm for 4 min. After centrifugation, the supernatant was discarded and the NSs were redispersed in 3 mL of toluene. $CsPbBr_3$ single crystals were grown following the work by Saidaminov et al.[31] Typically, CsBr (3 mmol) and $PbBr_2$ (6 mmol) were stirred in DMSO (3 mL) for one hour. Then the solution was filtered and the filtrate was transferred into a vial that was placed in a heating metallic block at 60 °C. The temperature was gradually increased. Upon reaching 100 °C, undesired yellow and orange crystals appeared. The solution was filtered, and the filtrate was transferred into a new vial preheated at 100 °C, and left undisturbed for 3 h. The formed crystals were washed with hot DMSO.

Optical PL Measurements: For the optical and radiometric measurements, the nanostructures were processed into films of comparable thickness (≈5 µm) by drop-casting solutions of the same concentration. The thickness or the BSC was ≈500 µm. The samples were excited at 3.06 eV using a pulsed diode laser (Edinburg Ins. EPL 405, 40 ps pulse width) and the emitted light was collected with a charged coupled device. Time-resolved PL was collected with a time-correlated single-photon counting unit (time resolution 600 ps) coupled to a monochromator and a photomultiplier tube. Nanostructured $CsPbBr_3$ crystals were deposited on a silica substrate by drop-casting from diluted toluene solutions. Temperature-controlled PL measurements were performed by mounting the samples in the variable temperature insert of a split-coil cryo-magnet with direct optical access. Φ_{PL} measurements were carried out in an integrating sphere by exciting the sample with a CW diode laser at 3.1 eV.

Ionizing Radiation Measurements: The samples were exposed to ionizing radiation using a Philips 2274 X-ray tube operating at 30 kV and 30 mA. X-rays were produced by a Bremsstrahlung mechanism due to the impact of electrons generated through thermionic effect and accelerated onto a tungsten target. The detection system consists of a monochromator (TRIAX 180 Jobin-Yvon) coupled to a charge-coupled device detector (Jobin-Yvon Spectrum One 3000) operating in the 190–1100 nm interval. The TSL and AG spectra were corrected for the spectral efficiency of the detection system. A 0.1 K s^{-1} heating rate was adopted in the TSL experiments. The penetration depth of the X-rays used in the experiments was approximately 2 µm (considering an attenuation factor of 5600 cm^{-1} at the employed energy), which was lower than the thickness of any of the samples. Therefore, reabsorption effects were considered to be comparable for all investigated systems.

Supporting Information

Supporting Information is available from the Wiley Online Library or from the author.

Acknowledgements

The authors acknowledge funding from the Italian Ministry of University and Research (MIUR) through grant "Dipartimenti di Eccellenza – 2017 Materials for Energy". L.M., S.B., J.S., and A.L.A. acknowledge financial support by the Italian Ministry of Research through the Italian-Israeli bilateral project "Artificial Intelligence and Data Management for Colloidal Quantum Dot Research (AI-4-QD)".

Open Access Funding provided by Universita degli Studi di Milano-Bicocca within the CRUI-CARE Agreement.

Conflict of Interest

The authors declare no conflict of interest.

Data Availability Statement

The data that support the findings of this study are available from the corresponding author upon reasonable request.

Keywords

$CsPbBr_3$, lead halide perovskites, nanocrystals, radiation detection, radioluminescence, scintillation, thermally stimulated luminescence, trapping

Received: May 22, 2021
Revised: July 7, 2021
Published online:

[1] a) M. Spahn, *Nucl. Instrum. Methods Phys. Res., Sect. A* **2013**, *731*, 57; b) X. Duan, J. Cheng, L. Zhang, Y. Xing, Z. Chen, Z. Zhao, *Nucl. Instrum. Methods Phys. Res., Sect. A* **2009**, *598*, 439; c) H. N. Chapman, P. Fromme, A. Barty, T. A. White, R. A. Kirian, A. Aquila, M. S. Hunter, J. Schulz, D. P. DePonte, U. Weierstall, R. B. Doak, F. R. N. C. Maia, A. V. Martin, I. Schlichting, L. Lomb, N. Coppola, R. L. Shoeman, S. W. Epp, R. Hartmann, D. Rolles, A. Rudenko, L. Foucar, N. Kimmel, G. Weidenspointner, P. Holl, M. Liang, M. Barthelmess, C. Caleman, S. Boutet, M. J. Bogan, J. Krzywinski, C. Bostedt, S. Bajt, L. Gumprecht, B. Rudek, B. Erk, C. Schmidt, A. Hömke, C. Reich, D. Pietschner, L. Strüder,

G. Hauser, H. Gorke, J. Ullrich, S. Herrmann, G. Schaller, F. Schopper, H. Soltau, K.-U. Kühnel, M. Messerschmidt, J. D. Bozek, S. P. Hau-Riege, M. Frank, C. Y. Hampton, R. G. Sierra, D. Starodub, G. J. Williams, J. Hajdu, N. Timneanu, M. M. Seibert, J. Andreasson, A. Rocker, O. Jönsson, M. Svenda, S. Stern, K. Nass, R. Andritschke, C.-D. Schröter, F. Krasniqi, M. Bott, K. E. Schmidt, X. Wang, I. Grotjohann, J. M. Holton, T. R. M. Barends, R. Neutze, S. Marchesini, R. Fromme, S. Schorb, D. Rupp, M. Adolph, T. Gorkhover, I. Andersson, H. Hirsemann, G. Potdevin, H. Graafsma, B. Nilsson, J. C. H. Spence, *Nature* **2011**, *470*, 73; d) R. P. Haff, *Sens. Instrum. Food Qual. Saf.* **2008**, *2*, 262; e) T. E. Schlesinger, J. E. Toney, H. Yoon, E. Y. Lee, B. A. Brunett, L. Franks, R. B. James, *Mater. Sci. Eng., R* **2001**, *32*, 103.

[2] a) C. Szeles, *Phys. Status Solidi B* **2004**, *241*, 783; b) C. Dujardin, E. Auffray, E. Bourret-Courchesne, P. Dorenbos, P. Lecoq, M. Nikl, A. N. Vasil'ev, A. Yoshikawa, R. Zhu, *IEEE Trans. Nucl. Sci.* **2018**, *65*, 1977.

[3] G. F. Knoll, *Radiation Detection and Measurement*, John Wiley & Sons, United States **2010**.

[4] a) D. Cao, G. Yang, *Mater. Today Commun.* **2020**, *24*, 101246; b) T. J. Hajagos, C. Liu, N. J. Cherepy, Q. Pei, *Adv. Mater.* **2018**, *30*, 1706956; c) A. Kamkaew, F. Chen, Y. Zhan, R. L. Majewski, W. Cai, *ACS Nano* **2016**, *10*, 3918; d) C. Liu, Z. Li, T. J. Hajagos, D. Kishpaugh, D. Y. Chen, Q. Pei, *ACS Nano* **2017**, *11*, 6422; e) R. M. Turtos, S. Gundacker, S. Omelkov, B. Mahler, A. H. Khan, J. Saaring, Z. Meng, A. Vasil'ev, C. Dujardin, M. Kirm, I. Moreels, E. Auffray, P. Lecoq, *npj 2D Mater. Appl.* **2019**, *3*, 37; f) R. M. Turtos, S. Gundacker, A. Polovitsyn, S. Christodoulou, M. Salomoni, E. Auffray, I. Moreels, P. Lecoq, J. Q. Grim, *J. Instrum.* **2016**, *11*, P10015; g) I. Villa, F. Moretti, M. Fasoli, A. Rossi, B. Hattendorf, C. Dujardin, M. Niederberger, A. Vedda, A. Lauria, *Adv. Opt. Mater.* **2020**, *8*, 1901348; h) E. Zanazzi, M. Favaro, A. Ficorella, L. Pancheri, G. F. D. Betta, A. Quaranta, *Phys. Status Solidi A* **2020**, *217*, 1900586.

[5] a) C. Ashworth, *Nat. Rev. Mater.* **2018**, *3*, 355; b) Q. Chen, J. Wu, X. Ou, B. Huang, J. Almutlaq, A. A. Zhumekenov, X. Guan, S. Han, L. Liang, Z. Yi, J. Li, X. Xie, Y. Wang, Y. Li, D. Fan, D. B. L. Teh, A. H. All, O. F. Mohammed, O. M. Bakr, T. Wu, M. Bettinelli, H. Yang, W. Huang, X. Liu, *Nature* **2018**, *561*, 88; c) F. Zhou, Z. Li, W. Lan, Q. Wang, L. Ding, Z. Jin, *Small Methods* **2020**, *4*, 2000506; d) F. Maddalena, L. Tjahjana, A. Xie, S. Z. Arramel, H. Wang, P. Coquet, W. Drozdowski, C. Dujardin, C. Dang, M. D. Birowosuto, *Crystals* **2019**, *9*, 88.

[6] a) Y. Li, W. Shao, X. Ouyang, Z. Zhu, H. Zhang, X. Ouyang, B. Liu, Q. Xu, *J. Phys. Chem. C* **2019**, *123*, 17449; b) H. Wei, J. Huang, *Nat. Commun.* **2019**, *10*, 1066.

[7] M. D. Birowosuto, D. Cortecchia, W. Drozdowski, K. Brylew, W. Lachmanski, A. Bruno, C. Soci, *Sci. Rep.* **2016**, *6*, 37254.

[8] a) Y. C. Kim, K. H. Kim, D.-Y. Son, D.-N. Jeong, J.-Y. Seo, Y. S. Choi, I. T. Han, S. Y. Lee, N.-G. Park, *Nature* **2017**, *550*, 87; b) W. Wei, Y. Zhang, Q. Xu, H. Wei, Y. Fang, Q. Wang, Y. Deng, T. Li, A. Gruverman, L. Cao, J. Huang, *Nat. Photonics* **2017**, *11*, 315.

[9] a) S. Yakunin, M. Sytnyk, D. Kriegner, S. Shrestha, M. Richter, G. J. Matt, H. Azimi, C. J. Brabec, J. Stangl, M. V. Kovalenko, W. Heiss, *Nat. Photonics* **2015**, *9*, 444; b) S. Shrestha, R. Fischer, G. J. Matt, P. Feldner, T. Michel, A. Osvet, I. Levchuk, B. Merle, S. Golkar, H. Chen, S. F. Tedde, O. Schmidt, R. Hock, M. Rührig, M. Göken, W. Heiss, G. Anton, C. J. Brabec, *Nat. Photonics* **2017**, *11*, 436.

[10] a) A. Xie, T. H. Nguyen, C. Hettiarachchi, M. E. Witkowski, W. Drozdowski, M. D. Birowosuto, H. Wang, C. Dang, *J. Phys. Chem. C* **2018**, *122*, 16265; b) V. B. Mykhaylyk, H. Kraus, V. Kapustianyk, H. J. Kim, P. Mercere, M. Rudko, P. Da Silva, O. Antonyak, M. Dendebera, *Sci. Rep.* **2020**, *10*, 8601.

[11] a) L. Protesescu, S. Yakunin, M. I. Bodnarchuk, F. Krieg, R. Caputo, C. H. Hendon, R. X. Yang, A. Walsh, M. V. Kovalenko, *Nano Lett.* **2015**, *15*, 3692; b) M. Imran, F. Di Stasio, Z. Dang, C. Canale, A. H. Khan, J. Shamsi, R. Brescia, M. Prato, L. Manna, *Chem. Mater.* **2016**, *28*, 6450; c) J. Shamsi, P. Rastogi, V. Caligiuri, A. L. Abdelhady, D. Spirito, L. Manna, R. Krahne, *ACS Nano* **2017**, *11*, 10206.

[12] G. Nedelcu, L. Protesescu, S. Yakunin, M. I. Bodnarchuk, M. J. Grotevent, M. V. Kovalenko, *Nano Lett.* **2015**, *15*, 5635.

[13] M. Nikl, A. Yoshikawa, *Adv. Opt. Mater.* **2015**, *3*, 463.

[14] J. Liu, B. Shabbir, C. Wang, T. Wan, Q. Ou, P. Yu, A. Tadich, X. Jiao, D. Chu, D. Qi, D. Li, R. Kan, Y. Huang, Y. Dong, J. Jasieniak, Y. Zhang, Q. Bao, *Adv. Mater.* **2019**, *31*, 1901644.

[15] Y. Zhang, R. Sun, X. Ou, K. Fu, Q. Chen, Y. Ding, L.-J. Xu, L. Liu, Y. Han, A. V. Malko, X. Liu, H. Yang, O. M. Bakr, H. Liu, O. F. Mohammed, *ACS Nano* **2019**, *13*, 2520.

[16] M. Gandini, I. Villa, M. Beretta, C. Gotti, M. Imran, F. Carulli, E. Fantuzzi, M. Sassi, M. Zaffalon, C. Brofferio, L. Manna, L. Beverina, A. Vedda, M. Fasoli, L. Gironi, S. Brovelli, *Nat. Nanotechnol.* **2020**, *15*, 462.

[17] a) A. Vedda, F. Moretti, M. Fasoli, M. Nikl, V. Laguta, *Phys. Rev. B* **2009**, *80*, 045104; b) M. Korzhik, G. Tamulaitis, A. N. Vasil'ev, in *Physics of Fast Processes in Scintillators*, (Eds: M. Korzhik, G. Tamulaitis, A. N. Vasil'ev), Springer International Publishing, Cham **2020**, p. 113.

[18] a) M. Nikl, V. V. Laguta, A. Vedda, *Phys. Status Solidi B* **2008**, *245*, 1701; b) P. Lecoq, in *Particle Physics Reference Library: Volume 2: Detectors for Particles and Radiation*, (Eds: C. W. Fabjan, H. Schopper), Springer International Publishing, Cham **2020**, p. 45.

[19] a) D. Totsuka, T. Yanagida, Y. Fujimoto, Y. Yokota, F. Moretti, A. Vedda, A. Yoshikawa, *Appl. Phys. Express* **2012**, *5*, 052601; b) O. Sidletskiy, A. Vedda, M. Fasoli, S. Neicheva, A. Gektin, *Phys. Rev. Appl.* **2015**, *4*, 024009.

[20] a) A. Dey, P. Rathod, D. Kabra, *Adv. Opt. Mater.* **2018**, *6*, 1800109; b) X. Lao, Z. Yang, Z. Su, Z. Wang, H. Ye, M. Wang, X. Yao, S. Xu, *Nanoscale* **2018**, *10*, 9949; c) M. Dendebera, Y. Chornodolskyy, R. Gamernyk, O. Antonyak, I. Pashuk, S. Myagkota, I. Gnilitskyi, V. Pankratov, V. Vistovskyy, V. Mykhaylyk, M. Grinberg, A. Voloshinovskii, *J. Lumin.* **2020**, *225*, 117346; d) V. S. Chirvony, S. González-Carrero, I. Suárez, R. E. Galian, M. Sessolo, H. J. Bolink, J. P. Martínez-Pastor, J. Pérez-Prieto, *J. Phys. Chem. C* **2017**, *121*, 13381.

[21] D. N. Dirin, L. Protesescu, D. Trummer, I. V. Kochetygov, S. Yakunin, F. Krumeich, N. P. Stadie, M. V. Kovalenko, *Nano Lett.* **2016**, *16*, 5866.

[22] a) K. Schötz, A. M. Askar, W. Peng, D. Seeberger, T. P. Gujar, M. Thelakkat, A. Köhler, S. Huettner, O. M. Bakr, K. Shankar, F. Panzer, *J. Mater. Chem. C* **2020**, *8*, 2289; b) Y. Liu, J. Wang, L. Zhang, W. Liu, C. Wu, C. Liu, Z. Wu, L. Xiao, Z. Chen, S. Wang, *Opt. Express* **2019**, *27*, 29124; c) M. Sebastian, J. A. Peters, C. C. Stoumpos, J. Im, S. S. Kostina, Z. Liu, M. G. Kanatzidis, A. J. Freeman, B. W. Wessels, *Phys. Rev. B* **2015**, *92*, 235210; d) S. V. Myagkota, A. V. Gloskovskii, A. S. Voloshinovskii, *Opt. Spectrosc.* **2000**, *88*, 538; e) S. T. Birkhold, E. Zimmermann, T. Kollek, D. Wurmbrand, S. Polarz, L. Schmidt-Mende, *Adv. Funct. Mater.* **2017**, *27*, 1604995; f) T. Yamada, Y. Yamada, Y. Nakaike, A. Wakamiya, Y. Kanemitsu, *Phys. Rev. Appl.* **2017**, *7*, 014001.

[23] a) A. Shinde, R. Gahlaut, S. Mahamuni, *J. Phys. Chem. C* **2017**, *121*, 14872; b) K. Wei, Z. Xu, R. Chen, X. Zheng, X. Cheng, T. Jiang, *Opt. Lett.* **2016**, *41*, 3821.

[24] K. Shibata, J. Yan, Y. Hazama, S. Chen, H. Akiyama, *J. Phys. Chem. C* **2020**, *124*, 18257.

[25] A. Rubino, A. Francisco-López, A. J. Barker, A. Petrozza, M. E. Calvo, A. R. Goñi, H. Míguez, *J. Phys. Chem. Lett.* **2021**, *12*, 569.

[26] M. A. Becker, R. Vaxenburg, G. Nedelcu, P. C. Sercel, A. Shabaev, M. J. Mehl, J. G. Michopoulos, S. G. Lambrakos, N. Bernstein, J. L. Lyons, T. Stöferle, R. F. Mahrt, M. V. Kovalenko, D. J. Norris, G. Rainò, A. L. Efros, *Nature* **2018**, *553*, 189.

[27] a) C. Rodà, A. L. Abdelhady, J. Shamsi, M. Lorenzon, V. Pinchetti, M. Gandini, F. Meinardi, L. Manna, S. Brovelli, *Nanoscale* **2019**, *11*, 7613; b) M. Lorenzon, L. Sortino, Q. Akkerman, S. Accornero, J. Pedrini, M. Prato, V. Pinchetti, F. Meinardi, L. Manna, S. Brovelli, *Nano Lett.* **2017**, *17*, 3844.
[28] S. W. S. McKeever, *Thermoluminescence of Solids*, Cambridge University Press, Cambridge **1985**.
[29] a) C. Hu, S.-P. Liu, M. Fasoli, A. Vedda, M. Nikl, X.-Q. Feng, Y.-B. Pan, *Opt. Mater.* **2015**, *45*, 252; b) R. Visocekas, M. Ouchene, B. Gallois, *Nucl. Instrum. Methods Phys. Res.* **1983**, *214*, 553; c) M. Nikl, A. Vedda, M. Fasoli, I. Fontana, V. V. Laguta, E. Mihokova, J. Pejchal, J. Rosa, K. Nejezchleb, *Phys. Rev. B* **2007**, *76*, 195121; d) A. Vedda, M. Fasoli, *Radiat. Meas.* **2018**, *118*, 86.
[30] A. C. Coleman, E. G. Yukihara, *Radiat. Meas.* **2018**, *117*, 70.
[31] M. I. Saidaminov, M. A. Haque, J. Almutlaq, S. Sarmah, X.-H. Miao, R. Begum, A. A. Zhumekenov, I. Dursun, N. Cho, B. Murali, O. F. Mohammed, T. Wu, O. M. Bakr, *Adv. Opt. Mater.* **2017**, *5*, 1600704.